

Why Channel-Centric Models are not Enough to Predict End-to-End Performance in Private 5G: A Measurement Campaign and Case Study

Nils Jörgensen

School of Industrial Engineering and Management
KTH Royal Institute of Technology
Stockholm, Sweden
Email: nilsjor@kth.se



Abstract—Communication-aware robot planning requires accurate predictions of wireless network performance. Current approaches rely on channel-level metrics such as received signal strength and signal-to-noise ratio, assuming these translate reliably into end-to-end throughput. We challenge this assumption through a measurement campaign in a private 5G industrial environment. We evaluate throughput predictions from a commercial ray-tracing simulator as well as data-driven Gaussian process regression models against measurements collected using a mobile robot. The study uses off-the-shelf user equipment in an underground, radio-shielded facility with detailed 3D modeling, representing a best-case scenario for prediction accuracy. The ray-tracing simulator captures the spatial structure of indoor propagation and predicts channel-level metrics with reasonable fidelity. However, it systematically over-predicts throughput, even in line-of-sight regions. The dominant error source is shown to be over-estimation of sustainable MIMO spatial layers: the simulator assumes near-uniform four-layer transmission while measurements reveal substantial adaptation between one and three layers. This mismatch inflates predicted throughput even when channel metrics appear accurate. In contrast, a Gaussian process model with a rational quadratic kernel achieves approximately two-thirds reduction in prediction error with near-zero bias by learning end-to-end throughput directly from measurements. These findings demonstrate that favorable channel conditions do not guarantee high throughput; communication-aware planners relying solely on channel-centric predictions risk overly optimistic trajectories that violate reliability requirements. Accurate throughput prediction for 5G systems requires either extensive calibration of link-layer models or data-driven approaches that capture real system behavior.

Index Terms—5G mobile communication, Throughput, MIMO, Channel models, Ray tracing, Gaussian processes

1 INTRODUCTION

Industrial automation is increasingly driven by mobile and collaborative robots that rely on reliable wireless connectivity for tasks such as supervision, teleoperation, and

Contributor role (CRediT) statement: Methodology, Investigation, and Data Curation: Awad AlNasrallah and Hoahui Meng; Supervision and Review & Editing: Prof. Fredrik Asplund and Dr. Ajay Kattepur; Resources: Stefan Rönngren. This research has received support from TECoSA. This work has been submitted to the IEEE for possible publication. Copyright may be transferred without notice, after which this version may no longer be accessible.

TABLE 1: List of abbreviations used in this paper.

5G	Fifth generation cellular network
EP5G	Ericsson Private 5G
GP	Gaussian process
GPR	Gaussian process regression
LOS	Line-of-sight
MAD	Median absolute deviation
MAE	Mean absolute error
MCS	Modulation and coding scheme
MIMO	Multiple-input multiple-output
RBF	Radial basis function
RI	Rank indicator
RMSE	Root mean squared error
RQ	Rational quadratic
RSRP	Reference signal received power
SBR	Shooting and bouncing rays
SD	Standard deviation
SINR	Signal-to-interference-plus-noise ratio
UE	User equipment

cloud/edge offloading. Fifth generation (5G) [1] systems are being positioned as a key enabler of this trend, promising high data rates, low latency, and quality-of-service (QoS) guarantees tailored to industrial use cases [2], [3], [4]. In factory environments, private 5G networks are being deployed to support autonomous mobile robots and automated guided vehicles, often operating in cluttered, metal-rich environments with strong multipath and blockage effects [5], [6], [7]. Consequently, the ability to accurately predict radio performance is crucial for both network design and the safe, reliable operation of mobile robots.

This need has given rise to *communication-aware* motion planning, an emerging paradigm in which predicted channel quality informs robot trajectories and task allocation [22]. Representative approaches include resilient communication-aware motion planners [23], joint motion-communication co-optimization [24], decentralized multi-robot coordination with inter-robot relay links [25], and radio-map-based path planning augmented with intelligent reflecting surfaces [26]. These methods typically employ parametric or learned models of channel quantities—such as

TABLE 2: Positioning of this study relative to prior work across key methodological dimensions.

Reference	Focus area	Indoor	Throughput	Measured	Predictive
Sheikh <i>et al.</i> [8]	Ray tracing simulation	✓	✓		✓
3GPP [9]	Stochastic channel model	✓			✓
Unger and Kuczmann [10]	Propagation model comparison				✓
Okano <i>et al.</i> [11]	5G field trial	✓	✓	✓	
5G-SMART [12]	Industrial 5G deployment	✓		✓	
Cantero <i>et al.</i> [13]	System-level simulation	✓	✓		✓
Vijayan <i>et al.</i> [14]	InF channel validation	✓		✓	✓
Polak <i>et al.</i> [15]	Industrial coverage	✓	✓	✓	
Hernangómez <i>et al.</i> [16]	AGV measurement dataset	✓		✓	
Tärneberg <i>et al.</i> [17]	Outdoors QoE measurement		✓	✓	
Santra <i>et al.</i> [18]	Propagation model validation			✓	✓
Coll-Perales <i>et al.</i> [19]	V2X latency modeling				✓
Lazar <i>et al.</i> [20]	5G KPI measurement		✓	✓	
Costa <i>et al.</i> [21]	Throughput prediction		✓		✓
This work	Industrial 5G robotics	✓	✓	✓	✓

received signal strength, path loss, or signal-to-interference-plus-noise ratio (SINR)—and treat them as cost terms or constraints in the planning problem, implicitly assuming that favorable channel conditions translate into adequate end-to-end performance.

Yet for autonomous robots, the metrics of ultimate interest are often end-to-end throughput and latency along a trajectory, rather than SINR or reference signal received power (RSRP) in isolation. While latency is central to many time-critical robotic applications, it can largely be controlled by preventing throughput from saturating; thus, accurate throughput prediction becomes a key enabler for latency-aware planning. In operational 5G systems, however, throughput depends not only on large-scale propagation but also on link adaptation, spatial multiplexing, precoding, scheduler behavior, and protocol overhead. Whether channel-level metrics reliably predict throughput is therefore an empirical question—one that has received surprisingly little attention.

This is not for lack of modeling tools. A substantial body of work has investigated 5G channel measurements and modeling across diverse scenarios—see [27], [28] for a comprehensive overview—leading to the development of standardized empirical stochastic models, such as 3GPP TR 38.901 [9]. In parallel, site-specific deterministic ray-tracing and hybrid models have been developed and validated for indoor factories and other complex environments [8], [14], [18], [29]. Complementing these physics-based approaches, data-driven methods—including machine-learning radio maps and Gaussian process (GP) models—have been proposed to predict path loss and related quantities such as coverage, signal strength, and theoretical spectral efficiency directly from measurements [30], [31], [32]. These tools are well established for predicting channel-level quantities; whether they—or any model—can accurately predict end-to-end throughput remains an open question.

1.1 Related Work

Validation of radio propagation models through measurement studies remains an active area of research. A com-

prehensive survey by Wang *et al.* [28] reviews the state of 5G channel measurements and models, covering diverse scenarios including massive multiple-input multiple-output (MIMO), millimeter-wave communications, and mobility. That survey identifies proper MIMO modeling as essential for 5G channels, emphasizing channel-level properties such as spherical wavefront and array non-stationarity. Crucially, however, the survey—and the body of work it reviews—focuses predominantly on channel-level quantities: path loss, delay spread, angular spread, and related propagation characteristics.

This channel-centric focus persists in subsequent work: comparisons between 3GPP-type stochastic models and ray-tracing in indoor factory-like environments typically report RSRP, SINR, or path loss as the primary indicators of model fidelity [8], [9], [10]. A growing number of measurement campaigns investigate 5G coverage, latency, and reliability for industrial scenarios, with a focus on system-wide performance indicators [11], [12], [13], [14], [15], [16]. Other studies emphasize outdoor or vehicular scenarios [17], [18], [19], [20], [21]. Table 2 positions this study relative to prior work across four methodological dimensions: (1) whether the study targets *indoor* industrial or factory-like environments; (2) whether *throughput* is evaluated as a key performance metric; (3) whether results are based on real-world *measurements* rather than pure simulation; and (4) whether the work develops or validates *predictive* models. Strikingly, no prior work evaluates a prediction model’s ability to provide actionable throughput estimates—whether predicted directly or derived from channel-level metrics such as SINR. The assumption that favorable channel conditions guarantee adequate throughput thus remains empirically untested, despite its centrality to communication-aware robot planning.

1.2 Purpose and Contributions

This paper addresses this gap through a single-site case study of downlink 5G throughput in a realistic industrial-like environment. We consider an underground, radio-shielded hall instrumented with a private 5G network and a mobile robot, and construct site-wide throughput maps

combining physics-based simulation and on-site measurements. A commercial ray-tracing simulation tool, configured with a 3GPP-compliant industrial channel model, is used to generate deterministic predictions, while GP models are trained on measurement data to provide data-driven throughput estimates. We then compare these approaches using a unified analysis framework and discuss their implications for communication-aware robot planning. Specifically, we address the following research questions:

RQ1: How accurately do physics-based ray-tracing simulators predict 5G throughput, and what are the significant sources of prediction error?

RQ2: How do data-driven Gaussian process regression (GPR) models compare to physics-based simulators for throughput prediction, and what factors influence their predictive performance the most?

Our results reveal that the physics-based ray-tracing simulator exhibits systematic over-prediction of throughput, driven primarily by over-estimation of sustainable MIMO spatial layers rather than inaccurate channel-level metrics. In contrast, using GPR achieves approximately two-thirds reduction in prediction error with near-zero bias, by learning end-to-end throughput behavior directly from measurements without explicit rank modeling. These findings indicate that communication-aware planners relying on channel-centric predictions may produce *overly optimistic* trajectory plans in regions with favorable SINR conditions.

The main contributions of this work are as follows:

- We conduct a robotic measurement campaign in a private indoor 5G deployment, collecting spatially dense downlink throughput, latency, and link-layer measurements in a complex, industrial-like environment, and make the dataset publicly available [33].
- We configure a state-of-the-art ray-tracing-based radio network planning tool for the same site, combining detailed 3D environment modeling, 3GPP-compliant indoor-factory channel settings, and parametric link modeling to obtain simulated throughput predictions.
- We develop data-driven throughput models using GPR, and train them on the collected measurements.
- We propose and apply a comparative analysis framework that quantifies the bias, accuracy, and variance of throughput predictions for both parametric and data-driven models.
- We highlight conditions under which channel-level metrics fail to predict throughput reliably, and discuss how these findings affect joint communication–motion planning for mobile robots.

1.3 Structure of this Paper

The remainder of this paper is organized as follows. Section 2 reviews industrial 5G, radio-channel modeling, and communication-aware motion planning. Section 3 presents the ray-tracing simulation, robotic measurement campaign, data-driven throughput modeling, and comparative analysis framework. Section 4 presents the results with some analysis. Section 5 discusses the results and puts forth relevant conclusions to the literature. Section 6 summarizes the conclusions of the study and outlines opportunities for future work.

2 BACKGROUND

This study centers on *throughput*—the volume of data successfully delivered over a wireless channel per unit time (e.g., Mbps)—as the primary performance metric. Throughput directly reflects the end-user experience and is sensitive to network resource allocation, particularly the dynamic assignment of physical resource blocks (PRBs) at the radio access network (RAN) level. Consequently, it serves as a natural objective for joint communication–motion planning, where robot trajectories may be optimized against predicted data-rate maps.

2.1 Radio Channel Modeling

Radio-channel models broadly fall into two categories. *Empirical* (statistical) models, such as those specified in 3GPP TR 38.901 [9], offer computational efficiency and require no detailed knowledge of the physical environment, but must be calibrated from measurement data. *Deterministic* models, such as ray-tracing, instead derive channel characteristics from explicit three-dimensional geometry and material properties, trading higher computational cost for site-specific accuracy without the need for prior measurements. For one part of this study, we employ a deterministic ray-tracing approach configured with 3GPP-compliant indoor-factory parameters.

Both approaches are fundamentally *channel-centric*: they predict quantities such as path loss or SINR, from which throughput is inferred through additional link-layer modeling. An alternative is to learn throughput maps directly from measurement data using data-driven regression techniques, bypassing the intermediate channel abstraction altogether.

2.2 Data-driven Modeling using GPR

GPR provides a probabilistic, non-parametric framework for modeling continuous spatial fields from data. Unlike physics-based or purely parametric models, GPR does not rely on explicit assumptions about the propagation environment or system behavior. Given training data, the model produces smooth spatial estimates together with predictive variances that quantify uncertainty—for example, in sparsely sampled or unobserved regions. These properties make GPR applicable to scenarios where multipath effects and adaptive link mechanisms are difficult to model deterministically.

In this study, GP models are trained using spatial measurement data consisting of a 2D-coordinate, a mean throughput, and the associated variability metric derived from repeated measurements (for implementation details, see Section 3.5). The training process fits the model to this dataset by adjusting its hyperparameters—such as signal variance, length scale, and noise variance—to maximize the marginal log-likelihood of the observations. Once trained, the GP model provides predictive means and variances for any query location, enabling extrapolation across unmeasured regions together with a calibrated estimate of prediction confidence.

2.3 Kernel Functions

Rather than specifying a fixed functional form, GP models define a prior distribution over functions

$$f(x) \sim \mathcal{GP}(m(x), k(x, x')), \quad (1)$$

where $m(x)$ is the mean function and $k(x, x')$ is the covariance kernel [34, Sec. 2.2]. The choice of kernel directly affects the covariance structure and thus the smoothness, length-scale behavior, and extrapolation properties of the trained models.

In this study, each evaluated kernel is formed as the product of a constant kernel and a stationary base kernel, with an additive white-noise kernel to capture measurement uncertainty, preventing the model from interpolating exactly through noisy observations and enabling smooth generalization between training points. This composite-kernel construction is inspired by [35, Chp. 2]. The general form can be written as

$$k(x, x') = \sigma_f^2 \cdot k_{\text{base}}(x, x') + \sigma_n^2 \cdot \delta(x, x'), \quad (2)$$

where σ_f^2 is the signal variance, scaling the base kernel $k_{\text{base}}(x, x')$; σ_n^2 is the white-noise level and $\delta(x, x')$ the Kronecker delta function. Below are the definitions of the three base kernels used in this study. They are common choices, as seen in [36], [37], [38].

Radial basis function (RBF)

The RBF (or “squared exponential”) kernel can be written as

$$k_{\text{RBF}}(x, x') = \exp\left(-\frac{\|x - x'\|^2}{2\ell^2}\right), \quad (3)$$

and measures the similarity between two points in space:

- if x and x' are very close, the kernel value is near 1;
- if they are far apart, the kernel value drops toward 0.

The characteristic length scale ℓ is optimized during the training process, and determines how quickly the correlation between points decays. This kernel assumes that the underlying function is *infinitely differentiable*, making it useful for modeling smooth and continuous phenomena.

Once-differentiable Matérn

The Matérn kernel is a generalization of the RBF kernel, controlled by a fixed smoothness parameter $\nu > 0$. Choosing $\nu = 1.5$ yields a *once-differentiable* covariance function, balancing moderately rough spatial variation with overall regularity. The resulting kernel is defined as

$$k_{\text{MI}}(x, x') = \left(1 + \frac{\sqrt{3}\|x - x'\|}{\ell}\right) \cdot \exp\left(-\frac{\sqrt{3}\|x - x'\|}{\ell}\right). \quad (4)$$

Rational quadratic (RQ)

The RQ is another smooth but flexible generalization of the RBF kernel that better captures multi-scale structure in data. It can be written as

$$k_{\text{RQ}}(x, x') = \left(1 + \frac{\|x - x'\|^2}{2\alpha\ell^2}\right)^{-\alpha}. \quad (5)$$

This kernel can be interpreted as an *infinite mixture* of RBF kernels, integrated over an inverse gamma distribution on

the squared length scale. The scale mixture parameter $\alpha > 0$ controls how wide that distribution of length scales is:

- small α : broad mixture, allows both short- and long-scale correlations, captures multi-scale structure;
- large α : narrow mixture, similar to RBF kernel.

This parameter α is co-optimized with ℓ during training.

3 METHODS

As outlined in Section 1.2, we conduct a single-site case study to compare a physics-based radio-channel simulator with a data-driven model for predicting 5G downlink throughput in a realistic industrial environment.

The study site is the KTH Reactor Hall, an underground facility that once housed Sweden’s first nuclear reactor [39]. Today, it features an Ericsson Private 5G (EP5G) network deployed as part of ExPECA (Experimental Platform for Edge Computing Applications) [40], a state-of-the-art research testbed providing high-performance edge computing and a range of networking capabilities. Fig. 1 shows the testbed site and the workspace in which the robot navigated during the measurement campaign.



Fig. 1: Photograph of the testbed site; an underground, radio-shielded facility used for edge- and cloud-computing research. Photo © 2008 Jann Lipka, used with permission. Source: 360Cities [41].

The ExPECA testbed was selected because it (1) integrates a private 5G core and radio equipment in a controlled environment, (2) provides a radio-shielded, large-volume indoor space that eliminates external interference, and (3) exposes container orchestration and isolated virtual networks, simplifying reproducible experiment deployment.

The Reactor Hall contains multiple radio dots, serving as base stations, at different elevations. This study intentionally uses a *single* high-mounted radio dot (approximately 8 m elevation; bottom-left position in the plan view; see Fig. 4) to create a more challenging coverage scenario and to stress-test prediction methods under complex indoor propagation.

The computational electromagnetics suite Altair Feko [42] was selected for deterministic radio propagation modeling because of its 3D CAD integration, native 5G air-interface support, versatile ray-tracing engine, and parametric antenna modeling utilities.

Fig. 2 illustrates the overall workflow of the study, where each stage corresponds to a subsequent section below. It outlines the sequential stages of the study—from modeling and radio configuration to simulations, robotic data collection,

and data-driven modeling—forming a unified framework for comparing model predictions with real-world measurements. The final step (shown in green) corresponds to Section 4, where we visualize and compare predictions against ground-truth measurements.

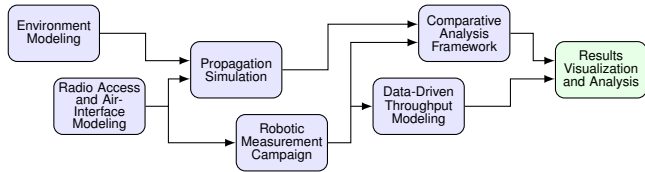


Fig. 2: Overview of the experimental and modeling workflow.

3.1 Environment Modeling

A detailed 3D model of the Reactor Hall was available from previous work by Adapt AB [43]. The model was created using a BLK360 3D scanner to capture the unique architecture of the facility with high precision. This specialized equipment generated point clouds with approximately 5 mm precision, which were then imported into computer design software for manual refinement to accurately represent architectural details and major fixtures. To reduce computational load while preserving key geometry, we simplified the original mesh for this study from approximately 1.1M polygons to just under 100 000 polygons prior to simulation. Pre-defined material properties were assigned to surfaces, and the resulting environment database was imported for propagation simulation.

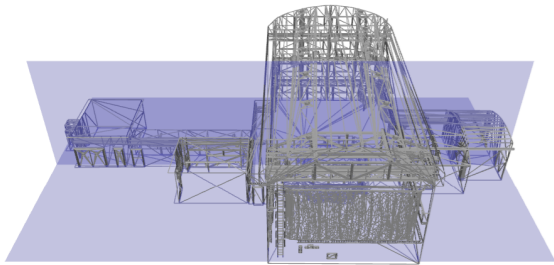


Fig. 3: 3D model of the KTH Reactor Hall imported into Altair Feko for radio propagation simulation.

Fig. 3 illustrates the simplified 3D geometry used for ray tracing, which preserved major reflectors and occluders while removing small-scale details that minimally affect large-scale propagation patterns.

3.2 Radio Access and Air-Interface Modeling

Building on the environment model, we configured the air-interface parameters and antenna placement to match the ExPECA deployment. Key configuration parameters include:

- 1) **Topology:** Four ceiling-mounted radio dots, which can be individually enabled or disabled.

- 2) **MIMO capabilities:** Each dot supports 4×4 MIMO downlink and 2×2 MIMO uplink.
- 3) **Carrier and numerology:** Band n78, center frequency $f_c = 3760$ MHz, channel bandwidth 80 MHz, and 3GPP numerology $\mu = 1$ (i.e., 30 kHz subcarrier spacing).
- 4) **TDD frame pattern:** Pattern 2, symbol sequence D-D-D-S-U, with Sub-pattern 2 (10:2:2); see [44] for details.

The modem used in this study reports only downlink metrics; consequently, the study is confined to downlink throughput measurements. However, because the uplink/downlink slot allocations are fixed, the effect of this restriction on the comparative analysis is expected to be limited.

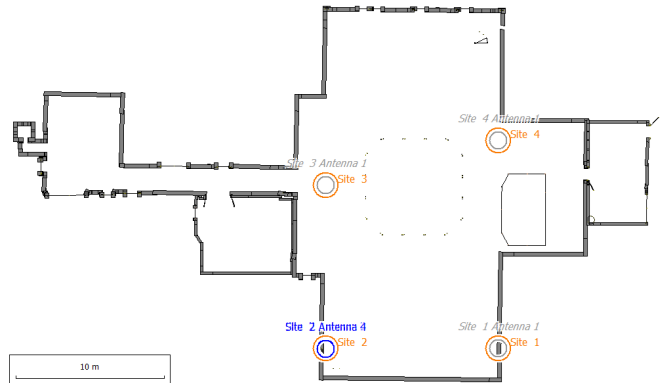


Fig. 4: Plan view of the Reactor Hall showing the placement of all radio dots in the environment. Only the highlighted dot (bottom-left) was enabled for the measurement campaign.

Fig. 4 shows the plan view with the location of the single active radio dot used for measurements. The dashed line in the center of the hall marks the “pit”—a recessed, non-traversable area where the nuclear reactor once operated, now enclosed by a protective railing.

3.3 Propagation Simulation

With the physical environment and air-interface configured, we employed the shooting and bouncing rays (SBR) method in Altair Feko for propagation prediction. SBR was selected over other methods for its ability to capture reflections, diffractions, transmissions, and scattering in complex indoor environments while balancing computational cost against simulation fidelity.

The simulation was executed on a 0.5 m horizontal grid map covering the accessible floor area. This generated spatial predictions of coverage and derived link-performance indicators, as well as predicted maximum throughput. Post-processing exported these predictions as heatmaps for subsequent comparison against measurements, with modulation and coding scheme (MCS) indices inferred via lookup from throughput fields for completeness of analysis.

3.4 Robotic Measurement Campaign

To validate the simulation predictions and provide training data for the data-driven models, we conducted a comprehensive measurement campaign using a modified Turtle-

Bot3 equipped with a Raspberry Pi 4 and a Waveshare 5G hat featuring a Quectel RM500Q-GL modem.

For experimental control, we configured isolated virtual networks on the ExPECA testbed to ensure measurement traffic traversed the 5G core network via a dedicated path with minimal hops between the robot and edge server. Husarnet [45], an IPv6-based overlay virtual private network (VPN), was used exclusively for control and management traffic, keeping measurement flows on the native EP5G data path to avoid introducing artificial performance artifacts resulting from tunneling.

To minimize confounding from small-scale fading and mobility, we employed a static sampling protocol. The robot advanced in discrete 0.5 m steps, stopping at each waypoint to collect:

- **Physical/link-layer metrics:** Radio channel metrics, MCS, and effective data layers using modem AT commands at 3 Hz; see Table 3.
- **Transport/network-layer metrics:** Downlink throughput via `iperf3` (TCP) and round-trip-time via ICMP pings at 1 Hz.

Multiple samples were taken at each waypoint to mitigate stochastic variability, and streams were synchronized by nearest-timestamp matching. Randomly selected throughput samples were sanity-checked against theoretical maxima for the network configuration, based on [46, Sec. 4] to detect gross anomalies.

TABLE 3: AT commands used for collecting radio metrics from the Quectel RM500Q-GL modem. For details, see [47].

AT command	Query
AT+QENG	Primary serving cell information
AT+QSINR	Signal-to-interference-plus-noise ratio
AT+QSRP	Reference signal received power
AT+QSRQ	Reference signal received quality
AT+QNWCFG=nr5g_csi	Channel state information
AT+QNWCFG=down	Average downlink throughput

To address potential localization drift in the large open space, we added small landmarks and performed occasional manual re-positioning when necessary. The hall was cleared of all other movable objects to match the 3D model geometry, and measurements were conducted during off-hours to minimize external interference.

The measurement campaign yielded approximately 9000 data points throughout the Reactor Hall. Following data cleansing to remove measurement anomalies, approximately 7000 valid samples remained for analysis. These samples were distributed across approximately 900 unique spatial locations. For each of these locations, we computed statistical summaries including mean, standard deviation, and other distributional parameters. The complete dataset, including raw measurements, processed statistics, and spatial coordinates, is publicly available [33].

3.5 Data-Driven Throughput Modeling

Using the collected measurement data, we trained GP models to estimate the spatial distribution of downlink throughput. Inputs x were the 2D spatial coordinates, and the response y was the measured downlink throughput. Because

measurement uncertainty varies spatially—e.g., due to differing sample counts or local conditions—we employ *heteroscedastic* noise modeling by providing the per-point standard deviation term individually for each training location. The measurement dataset was split into 70% training and 30% test using random sampling; multiple random seeds were used to assess variability across splits. The regression problem was implemented using the `scikit-learn` library [48].

Three stationary covariance kernels were evaluated: RBF, Matérn, and RQ; see Section 2.3 for more details. For each kernel and random seed, hyperparameters were optimized by maximizing the log marginal likelihood with five random restarts to mitigate local optima. To improve convergence, hyperparameter initial guesses were derived empirically from each training set:

- σ_f^2 : measurement variance across all training data,
- ℓ : median L^2 -distance to 10th nearest neighbor,
- σ_n^2 : median per-point measurement variance.

Finally, trained models were used to generate spatial throughput predictions over the same 0.5 m grid as the simulation for direct comparison.

3.6 Comparative Analysis Framework

All measurements and predictions were aligned in a common coordinate frame via nearest-neighbor matching (threshold: 0.5 m). The signed error is defined as $e_i = \hat{y}_i - y_i$, where y_i is the measured throughput and \hat{y}_i the model prediction (positive indicates over-prediction), and $|e_i|$ denotes the absolute error. Where relevant, the relative error is defined as $e_i^{\text{rel}} = e_i/y_i$ and is reported in percent. We evaluate performance using a statistical scorecard, grouped into the following categories.

Category 1: Bias (Directional Tendency):

We begin by quantifying systematic directional error—whether predictions tend to be optimistic (over-prediction) or pessimistic (under-prediction).

- Median error
- Mean over-/under-prediction magnitudes
- Over-/under-prediction rates (percent)
- Maximum over-/under-prediction magnitudes

Category 2: Accuracy (Central Tendency of Error Size):

Having established directional tendencies, we next measure the typical magnitude of discrepancy regardless of sign.

- Mean absolute error (MAE)
- Root mean squared error (RMSE)

Category 3: Variability (Deviations and Tail Risk):

Building on central-tendency accuracy, we then characterize dispersion and tail risk to assess the reliability and spread of fluctuating conditions. Tail-focused statistics highlight rare but consequential deviations and support risk-aware decisions and worst-case planning.

- Sample standard deviation of signed errors.
- Sample standard deviation of absolute errors.
- Median absolute deviation (MAD).
- Percentiles of absolute error: $P_{90}(|e|)$ and $P_{95}(|e|)$.

Visualization of Results

We complement the summary metrics by examining statistical distributions of the signed and absolute errors using histograms, which quantify central tendency, dispersion, skewness, and tail behavior, and make outliers explicit.

In parallel, spatial heatmaps reveal geographically localized error patterns across environmental contexts (e.g., corners, corridors, and occluded areas), supporting qualitative assessment of the operational conditions under which different predictors perform well or poorly. The scientific color maps `batlow` and `vik` from [49] are used in this study to prevent visual distortion of the data and the exclusion of readers with color-vision deficiencies.

The subsequent Results section applies this comparative framework to evaluate all three prediction methods—physics-based simulation, data-driven GPR models, and measurements—using the metrics and visualizations defined above.

4 RESULTS

This section presents the empirical and modeling results obtained from three complementary approaches: the physics-based SBR simulator, on-site physical measurements, and data-driven GPR models. We first provide a qualitative assessment of the site-wide 2D prediction maps to identify systematic patterns and failure modes, and subsequently present a more comprehensive statistical comparison using error distributions and a quantitative scorecard of summary metrics. The analysis follows a systematic progression through the following stages:

- Section 4.1: Empirical comparison between simulation and measurements, including qualitative error analysis.
- Section 4.2: Investigation into the physics-based simulator, focusing on link-layer phenomena.
- Section 4.3: Evaluation of data-driven GPR throughput prediction, with kernel-specific comparisons.
- Section 4.4: Statistical comparison across all methods, including error distributions and summary metrics.
- Section 4.5: Summary of key findings.

We begin with the key operational metric—downlink throughput—and then interpret the result via the link-adaptation variables (MCS and spatial layers). This ordering reflects that throughput is the end-to-end quantity of interest, whereas other simulated metrics explain *why* the simulator succeeds or fails at a given location.

4.1 Parametric (Physics-Based) Simulation Results

The simulated throughput field, shown in Fig. 5a, reveals a clear structure driven by the environment’s large-scale geometry. The open central hall exhibits peak rates up to approximately 740 Mbit/s under the configured 80 MHz carrier and nominal 4-layer transmission. In contrast, obstructed regions—such as the far left corridor behind multiple concrete walls and the right-hand corner near a large wooden structure—display pronounced degradation. This pattern aligns with expectations: line-of-sight (LOS) areas yield strong performance, while heavily shadowed or penetration-limited zones exhibit substantial attenuation.

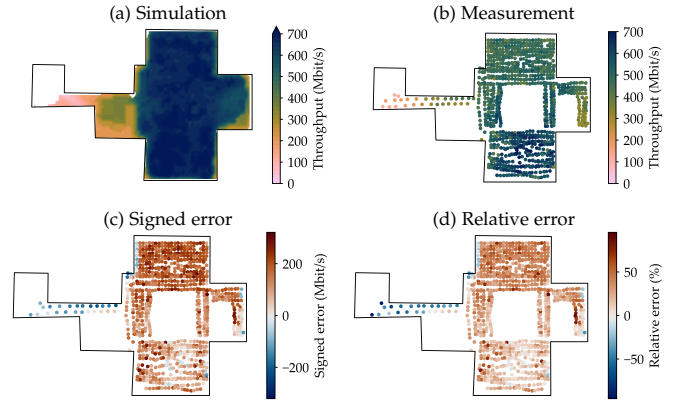


Fig. 5: Site-wide 2D map of throughput: simulation vs. measurement and associated errors. A positive error indicates over-prediction.

Comparing these simulated predictions against measurements using the nearest-neighbor pairing defined in Section 3 reveals a substantial mismatch. To quantify the simulator–measurement discrepancy, we compile a scorecard of throughput errors computed over all paired locations; see Section 3. Errors are defined so that positive values indicate over-prediction. Table 4 summarizes bias, accuracy, and variability statistics.

TABLE 4: Throughput error scorecard (simulation vs. measurement).

Metric	Value	Unit
Bias		
Median error	144.8	Mbit/s
Mean over-prediction magnitude	150.9	Mbit/s
Mean under-prediction magnitude	74.9	Mbit/s
Over-prediction rate	92.4	%
Under-prediction rate	7.6	%
Maximum over-prediction magnitude	321.0	Mbit/s
Maximum under-prediction magnitude	221.2	Mbit/s
Accuracy		
Mean absolute error (MAE)	145.1	Mbit/s
Root mean squared error (RMSE)	161.1	Mbit/s
Variability		
Standard deviation (SD) of signed error	89.8	Mbit/s
Standard deviation (SD) of absolute error	69.9	Mbit/s
Median absolute deviation (MAD)	54.6	Mbit/s
90 th percentile of absolute error, $P_{90}(e)$	232.5	Mbit/s
95 th percentile of absolute error, $P_{95}(e)$	253.7	Mbit/s

As summarized in Table 4, the average error metrics are in the order of approximately 100 Mbit/s, corresponding to roughly 10–15% relative error, given typical throughput levels in this environment.

4.2 Investigating Throughput Discrepancies

More importantly, the regional error pattern across the floorplan, visible in Fig. 5, shows a clear trend: agreement is best near the active radio dot (below the central pit), remains reasonable in the far left corridor and right corner, yet degrades above the pit where path length is greatest and multipath complexity increases.

To better understand these discrepancies, we next examine the link-adaptation mechanism. We first compare the simulator’s expected MCS with the one actually selected by the radio, i.e., the value reported by the user equipment (UE) during the measurement interval.

4.2.1 Why compare MCS rather than SINR?

In the simulator, transitions between MCS indices are governed by fixed SINR thresholds applied at each sampled location: an MCS is selected if the local SINR exceeds the minimum threshold for that MCS. In a standards-compliant system, the selected MCS reported by the UE reflects the system’s practical mapping from channel conditions into a stable, usable choice of modulation and coding—capturing feedback, reporting, and short-term adaptation—rather than an instantaneous theoretical optimum based solely on SINR. Because throughput depends directly on the used MCS together with the chosen number of spatial layers, a comparison of the *measured* MCS provides a more meaningful diagnostic of throughput discrepancies than raw SINR values alone. We therefore begin by evaluating how well the simulator predicts MCS, then proceed to examine spatial layer selection.

4.2.2 MCS: Pessimistic but Directionally Correct

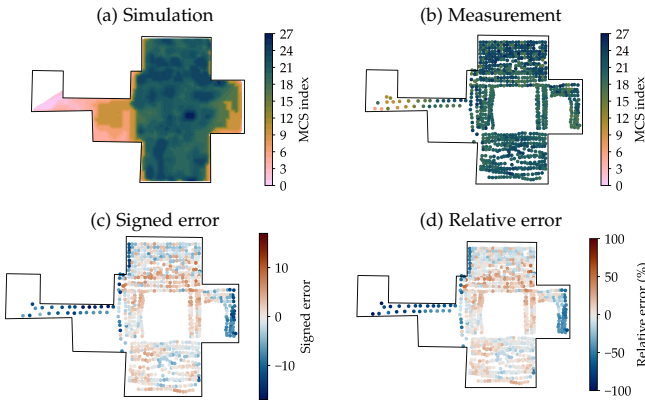


Fig. 6: Site-wide 2D map of modulation and coding scheme (MCS) index (0–27): simulation vs. measurement and associated errors. A positive error indicates over-prediction.

Fig. 6 contrasts the simulated and measured MCS fields, revealing a stronger overall agreement. In the strong-signal region below the pit, MCS agrees closely, indicating that the simulator captures the high-performance operating point. In areas impacted by partial shadowing and complex multipath, the behavior is mixed: the simulator tends to *overestimate* MCS in some more distant regions, but it *underestimates* MCS substantially in the far left corridor and in the right-hand corner with heavy obstruction. Overall, despite a mild pessimism bias in difficult regions, the simulated MCS tracks the overall structure of the measured MCS reasonably well. Importantly, this suggests that MCS prediction (and thus SINR) itself is *not* the main driver of the large throughput error reported in Table 4.

4.2.3 MIMO Spatial Layers: The Main Source of Mismatch

Having established that MCS prediction is largely adequate, we now turn to spatial layer selection—the decisive factor behind throughput mismatch. The number of *spatial layers* is formally reported by the UE as the rank indicator (RI), which indicates how many independent data streams (also called data layers) can be transmitted simultaneously over the radio channel. Higher RI values enable greater spatial multiplexing and thus higher throughput, with a maximum of four layers in our test configuration.

It is important to note that in 5G systems, the number of utilized layers *can* be strictly lower than the instantaneous channel rank reported as RI. This occurs when the scheduler limits layers to satisfy low traffic demand, improve power and spectrum efficiency, or mitigate inter-user interference and congestion. In our study, however, we imposed a sustained downlink load over an isolated EP5G data path using a single active radio dot with no other scheduled traffic (see Section 3). Given this controlled setup, the likelihood of demand- or congestion-driven layer throttling is exceedingly low, allowing us to interpret observed RI values as reflecting genuine channel capacity rather than scheduler constraints.

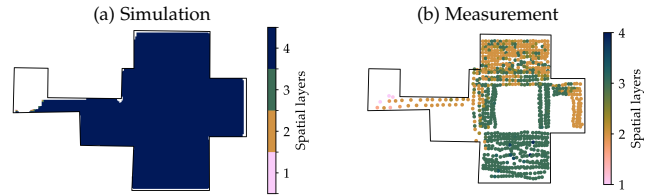


Fig. 7: Site-wide 2D map of utilized spatial layers; reported as rank indicator (RI).

As can be seen in Fig. 7, the simulator predicts a *uniform* $RI = 4$ (four spatial layers) throughout the hall, with only small localized reductions near the far end of the corridor; by contrast, the measured RI exhibits clear adaptation:

- $RI \geq 3$ (three spatial layers) in strong-signal LOS regions (with only a few locations reaching four layers),
- $RI \approx 2$ (two spatial layers) in further-away regions and under moderate conditions,
- $RI = 1$ (single spatial layer) in heavily attenuated areas (e.g., the far left corridor).

Because throughput scales with both spectral efficiency (via MCS) *and* spatial multiplexing (via RI), overpredicting the available spatial rank inflates the simulated throughput even when the MCS is predicted conservatively. This explains the seemingly paradoxical trend where throughput greatly disagrees in LOS regions, despite the predicted MCS being close. Additionally, measurements display non-integer average RI at some locations, reflecting rapid rank switching over the sampling window; indicating that the sustainable spatial rank is strongly location-dependent and varies with small-scale fading.

4.2.4 Summary

The analysis reveals that the physics-based simulator captures the general structure of indoor propagation—high

performance in LOS regions, degradation under heavy shadowing—and predicts MCS with reasonable fidelity, albeit with conservative bias in the most challenging areas. However, the dominant error mechanism is *over-prediction of sustainable rank*, which inflates simulated throughput where the real system reduces the number of spatial layers. This assessment is consistent with the overall throughput error illustrated in Fig. 5: the highest overestimation occurs above the pit, while better agreement emerges near the radio dot and in severely shadowed zones where operational rank is inherently low.

4.3 Data-Driven Throughput Prediction

Having identified the limitations of the physics-based approach, we now turn to a purely data-driven alternative that predicts downlink throughput directly, for a given 2D location, without explicit modeling of propagation physics.

With the composite kernel formulation described in Section 2.3—including the white noise term for regularization—all three kernels produce qualitatively similar predictions that capture both large-scale propagation trends and local variations. Fig. 8 shows representative GPR predictions; the three kernels yield visually comparable maps for mean throughput.

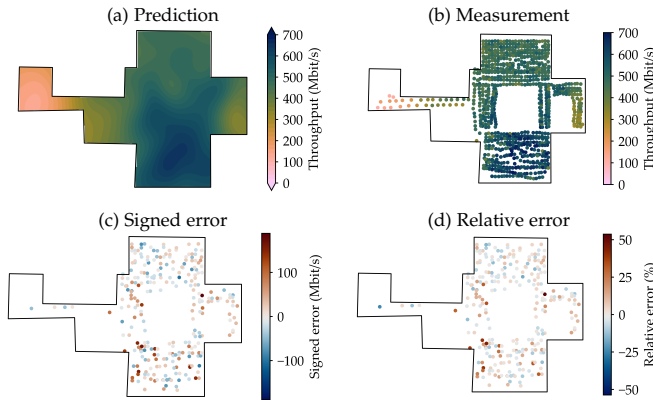


Fig. 8: Site-wide 2D map of throughput: GPR prediction (RQ kernel) vs. measurement and associated error.

While mean predictions are nearly indistinguishable across kernels, the spatial distribution of predictive uncertainty reveals clear differences in how each kernel represents confidence in unobserved regions. Fig. 9 presents a comparative analysis of predictive uncertainty, visualized as posterior standard deviation, across the three kernel functions and contrasted with the empirical throughput variability observed in measurements.

It can be seen that the kernels exhibit modest differences in their ability to differentiate uncertainty spatially:

- **RBF**: Relatively uniform posterior variance across the environment, with only slight increase around the central pit and limited localized low-uncertainty regions.
- **Matérn**: Somewhat increased posterior variance in sparsely measured regions (e.g., around the pit), with emerging areas of lower uncertainty that begin to align with reduced measurement variability.

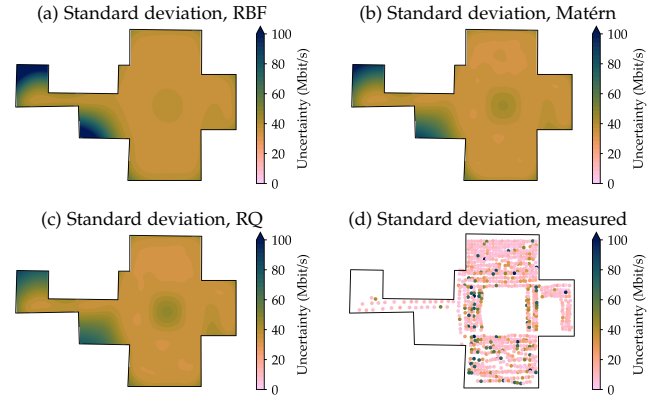


Fig. 9: Site-wide 2D map of predictive uncertainty (posterior standard deviation): GPR models compared with measured throughput variability. All color maps use the same scale for direct comparability.

- **RQ**: More noticeable spatial differentiation of uncertainty, with moderately elevated variance in unmeasured regions, and slightly larger coherent areas of low predicted uncertainty where empirical measurement variability is consistently low.

This progression reflects the kernels’ structural flexibility: the RQ kernel’s scale-mixture formulation better captures the multi-scale spatial structure of indoor propagation, producing uncertainty estimates that more faithfully track the underlying measurement variability. For applications requiring calibrated uncertainty estimates, such as risk-aware planning, it is clear that the kernel choice becomes relevant; we discuss this further in Section 5.

4.4 Statistical Comparison Across Methods

To compare methods in a way that is visually interpretable and statistically sound, we examine the distributions of mean throughput error using per-method histograms with common bin edges and shared axes (Fig. 10). All histograms are normalized as probability density functions (PDFs), i.e., counts are scaled so that the total area is one. This normalization removes the visual dependence on sample size and makes the shapes directly comparable across methods: biases manifest as shifts of mass away from zero, spread reflects variability, and heavy tails indicate outliers. Because the GPR models are trained and evaluated on a 30% subsample whereas the simulator is compared against all measured points, it is important to note that PDF estimates from smaller sample sizes may exhibit higher variance and appear noisier, particularly in the tails. Complementing the visual comparison, Table 5 reports a quantitative scorecard that aggregates the same information into interpretable summary statistics.

The bias group captures location and asymmetry, the accuracy group reports overall error levels, and the variability group summarizes dispersion and tail behavior. Together, the figure and the table provide complementary views: distributional shape for intuition and side-by-side numbers for precise comparison.

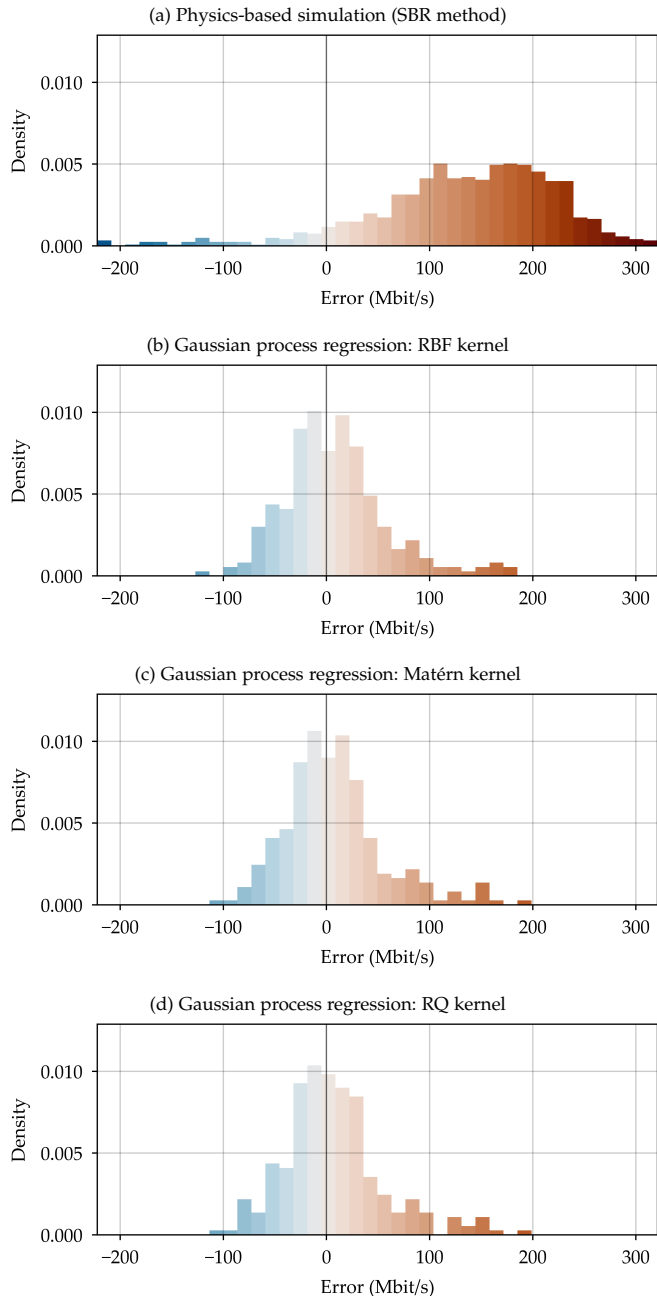


Fig. 10: Throughput error histograms across methods, using common bin edges and shared axes. All histograms are PDF-normalized, making shapes directly comparable across datasets of different sizes.

4.5 Summary

Compared with the physics-based simulator, GPR-based predictors yield consistently lower error and bias across all metrics: the median error is near zero, MAE and RMSE are reduced by roughly two-thirds, the 90th and 95th percentiles are markedly smaller, and the worst-case magnitudes are also diminished. This improvement is visually evident in Fig. 10, where the GPR error distributions are centered near zero with significantly narrower spread, contrasting sharply with the simulator’s pronounced positive skew and elongated right tail reflecting systematic over-prediction.

TABLE 5: Throughput error scorecard: all methods.

Metric	Sim	RBF	M1	RQ	Unit
Bias					
Median error	144.8	2.5	1.5	1.7	Mbit/s
Mean over-pred.	150.9	42.6	42.0	41.6	Mbit/s
Mean under-pred.	74.9	30.7	29.2	29.5	Mbit/s
Over-pred. rate	92.4	52.2	51.5	51.9	%
Under-pred. rate	7.6	47.8	48.5	48.1	%
Max over-pred.	321.0	180.0	186.7	188.7	Mbit/s
Max under-pred.	221.2	114.3	102.0	100.1	Mbit/s
Accuracy					
MAE	145.1	36.9	35.8	35.8	Mbit/s
RMSE	161.1	49.6	49.0	49.0	Mbit/s
Variability					
SD (signed)	89.8	49.0	48.4	48.5	Mbit/s
SD (absolute)	69.9	33.1	33.4	33.5	Mbit/s
MAD	54.6	26.8	23.9	24.4	Mbit/s
$P_{90}(e)$	232.5	77.6	77.9	78.6	Mbit/s
$P_{95}(e)$	253.7	98.0	99.0	99.5	Mbit/s

5 DISCUSSION

This study set out to evaluate whether physics-based simulation and data-driven modeling can reliably predict fifth generation (5G) [1] downlink throughput for communication-aware robotic planning in industrial environments. We now interpret the comparative results to answer RQ1 and RQ2, explain the mechanisms behind observed performance differences, and assess implications for communication-aware planning.

5.1 Summary of Key Findings

We structure our findings around the two research questions posed in Section 1.

RQ1: Physics-Based Simulation Accuracy

The physics-based shooting and bouncing rays (SBR) simulator successfully captures the spatial structure of indoor 5G propagation, correctly predicting high modulation and coding scheme (MCS) indices in line-of-sight (LOS) regions with degradation in shadowed areas. However, it exhibits systematic throughput overestimation: the model consistently over-predicts at 92% of measured locations, with a median error of approximately 145 Mbit/s. The dominant error source is over-prediction of MIMO spatial layers; the simulator predicts near-uniform four-layer transmission, while measurements reveal substantial adaptation. Generally, we see three or more layers only in strong LOS regions, two layers in moderate conditions, and single-layer fallback in heavily attenuated areas. This discrepancy directly inflates predicted throughput, as it scales multiplicatively with spectral efficiency and spatial multiplexing gain. Notably, while prior surveys have identified proper MIMO modeling as essential for 5G channels—emphasizing channel-level properties such as spherical wavefront and array non-stationarity [28]—our results demonstrate that even modest single-user MIMO configurations (four antennas) exhibit substantial discrepancies between predicted and realized spatial multiplexing gain. This is a link-layer phenomenon that channel-centric models do not capture.

Three modeling simplifications likely contribute to this optimistic spatial rank prediction:

- 1) The simulator likely employs idealized antenna patterns and simplified beam management, neglecting the vendor-specific trade-offs between analog and digital precoding stages inherent in hybrid beamforming architectures [50].
- 2) It likely assumes near-ideal inter-stream orthogonality, employing simplified inter-stream interference models that do not fully capture subspace overlap and interference arising in realistic indoor multipath [51].
- 3) It does not account for the closed-loop feedback and scheduling logic that jointly adjusts MCS and rank indicator (RI) under instantaneous channel and load conditions; accurate modeling of PMI and RI reporting mechanisms can significantly affect predicted performance [51].

RQ2: Data-Driven GPR Performance

The GPR models, when properly configured, achieve substantially better predictive performance. When looking at the error, relative to the simulator, GPR achieves:

- elimination of bias (median error near zero, close to 50–50 split between over- and under-prediction);
- approx. two-thirds reduction in MAE and RMSE;
- up to 60 % reduction in the 90th and 95th percentiles;
- approx. 25 % reduction in maximum error magnitudes.

One key factor enabling this performance is proper noise modeling through the white noise term in the composite kernel formulation. When omitted, all kernels exhibit underfitting of large-scale trends while overfitting local variations. With proper noise modeling, the three evaluated kernels produce statistically indistinguishable mean predictions—kernel choice becomes secondary to noise regularization for point prediction accuracy.

However, kernels differ in their posterior uncertainty structure, though the effect is subtle. Broadly speaking, the radial basis function (RBF) kernel yields nearly uniform posterior variance, whereas the rational quadratic (RQ) kernel produces variance fields that spatially track empirical measurement variability to a larger degree. For risk-aware planning applications that incorporate uncertainty bounds, this distinction may become practically important.

5.2 Implications for Communication-Aware Planning

Both methodologies produce spatially structured predictions suitable for integration with planning algorithms, but exhibit fundamental limitations that persist even under near-ideal experimental conditions.

Physics-based simulation provides physics-grounded extrapolation across the entire environment, including unmeasured regions. However, the substantial prediction errors—despite near-laboratory conditions with detailed geometry, controlled environment, and no external interference—reveal inherent limitations for end-to-end throughput prediction. The systematic spatial rank overprediction stems from the modeling simplifications identified in Section 5.1, and these limitations are unlikely to be resolved in the near future. First, accurately modeling hybrid beamforming requires capturing the intricate trade-offs between analog and digital precoding stages, RF chain constraints, and beam management procedures that

vary across vendors and deployments [50]—information that is rarely disclosed. Second, realistic inter-stream interference modeling demands computationally intensive matrix operations and receiver algorithms (e.g., MMSE-IRC) that many ray-tracing simulators simplify or omit entirely [51]. Third, closed-loop CSI feedback mechanisms—including PMI and RI selection algorithms—are proprietary, implementation-specific, and interact with real-time scheduling decisions that cannot be replicated without access to vendor firmware [51]. Together, these factors create a persistent gap between simulated and realized spatial multiplexing gain that per-deployment calibration cannot fully bridge without undermining the primary advantage of simulation-based prediction. In realistic industrial deployments with incomplete geometry, dynamic obstacles, and time-varying interference, physics-based predictions may exhibit substantially larger deviations.

These findings also temper assumptions underlying much prior work on communication-aware motion planning. Existing approaches—including resilient planners [23], motion–communication co-optimization [24], and radio-map-based indoors planning [26]—typically treat signal-to-interference-plus-noise ratio (SINR) or received signal strength as the primary optimization objective, implicitly assuming that favorable channel conditions translate reliably into high throughput. Our results challenge this channel-centric paradigm: the physics-based simulator achieved reasonable SINR (and thus MCS) predictions, yet throughput errors remained substantial due to spatial rank overprediction. This suggests that planners optimizing purely for SINR may fail to deliver expected throughput in practice, particularly in MIMO systems where spatial multiplexing gain depends on hybrid beamforming architectures, inter-stream interference suppression, and closed-loop rank adaptation—none of which are captured by channel-level metrics. Because the underlying modeling challenges are structural rather than merely a matter of calibration or improved channel estimation, this gap is unlikely to be closed through incremental refinements to physics-based simulators. For robust communication-aware planning, end-to-end performance prediction—rather than channel-level proxies—should be the target metric.

While data-driven methods offer an alternative path toward end-to-end throughput prediction, they introduce their own operational challenges which have to be addressed. GPR achieves lower error by learning system behavior directly from measurements, but has cubic-time computational complexity that becomes costly as measurement campaigns scale. More critically, GPR models are conservative and slow to adapt: regions with strong historical measurement density exhibit high confidence in outdated predictions even after physical modifications, requiring extensive remeasurement to override prior beliefs. This may create an unsustainable operational burden as the environment or network configuration evolves. Neither approach therefore provides a fully satisfactory solution for reliable throughput prediction under realistic operational conditions.

6 CONCLUSION

This study compared physics-based and data-driven approaches for predicting 5G downlink throughput in the KTH Reactor Hall—an underground facility equipped with an Ericsson Private 5G (EP5G) network and edge-computing testbed. A robotic platform collected spatially distributed measurements to validate predictions from a ray-tracing simulator as well as Gaussian process regression (GPR) models with three distinct kernel types. The measurement dataset is publicly available to support reproducibility and future research [33].

The central finding challenges a common assumption in communication-aware robotics: that favorable channel conditions—as captured by SINR or received signal strength—translate reliably into high throughput. The physics-based simulator achieved reasonable MCS predictions yet systematically over-predicted throughput due to optimistic MIMO spatial rank assumptions. This indicates that planners optimizing channel-level metrics may not achieve expected throughput in practice, highlighting the need for end-to-end performance prediction rather than intermediate channel proxies. The GPR models reduced prediction error by approximately two-thirds and eliminated systematic bias, demonstrating that data-driven approaches can capture end-to-end system behavior that physics-based simulators miss. Notably, all three kernels produced statistically indistinguishable mean prediction accuracy; however, they differed substantially in their posterior uncertainty structure, with the RQ kernel best tracking empirical measurement variability. Both approaches have practical trade-offs: physics-based simulation requires extensive calibration and access to proprietary link-adaptation logic, while data-driven methods require substantial measurement data and adapt slowly to environmental changes.

Future work should explore hybrid approaches combining physics-based priors with data-driven refinement, investigate scalable machine learning methods for larger deployments, and develop online adaptive methods that update predictions during robot operation. For risk-aware planning applications, attention should be given to covariance kernel selection, as it determines the degree with which the posterior variance aligns with empirical data variability. Integration with intent-driven autonomous network management and digital network twin frameworks may offer promising directions for bridging the gap between prediction and reliable planning.

REFERENCES

- [1] 3GPP, “System architecture for the 5G system,” Sophia Antipolis, France, Technical Specification 23.501, Sep. 2025.
- [2] 5G-ACIA, “5G QoS for industrial automation,” 5G Alliance for Connected Industries and Automation, Frankfurt am Main, Germany, White Paper, Nov. 2021.
- [3] A. Mahmood, S. F. Abedin, T. Sauter, M. Gidlund, and K. Landernäs, “Factory 5G: A review of industry-centric features and deployment options,” *IEEE Industrial Electronics Magazine*, vol. 16, no. 2, pp. 24–34, Jun. 2022. DOI: 10.1109/MIE.2022.3149209
- [4] M. Wollschlaeger, T. Sauter, and J. Jasperneite, “The future of industrial communication: Automation networks in the era of the internet of things and industry 4.0,” *IEEE Industrial Electronics Magazine*, vol. 11, no. 1, pp. 17–27, Mar. 2017. DOI: 10.1109/MIE.2017.2649104
- [5] 5G-ACIA, “Key 5G use cases and requirements,” 5G Alliance for Connected Industries and Automation, Frankfurt am Main, Germany, White Paper, May 2020.
- [6] 5G-SMART, “Report on the development of 5G use cases,” Deliverable 4.3, 2021.
- [7] K.-C. Chen, S.-C. Lin, J.-H. Hsiao, C.-H. Liu, A. F. Molisch, and G. P. Fettweis, “Wireless networked multirobot systems in smart factories,” *Proceedings of the IEEE*, vol. 109, no. 4, pp. 468–494, Apr. 2021. DOI: 10.1109/JPROC.2020.3033753
- [8] M. U. Sheikh, K. Ruttik, R. Jäntti, and J. Hämäläinen, “Blockage and ray tracing propagation model in 3GPP specified industrial environment,” in *2021 International Conference on Information Networking (ICOIN)*, Jan. 2021, pp. 397–402. DOI: 10.1109/ICOIN50884.2021.9333909
- [9] 3GPP, “Study on channel model for frequencies from 0.5 to 100 GHz,” Sophia Antipolis, France, Technical Report 38.901, Mar. 31, 2022.
- [10] T. I. Unger and M. Kuczmann, “The impact of terrain sampling density on 5G NR-V2X downlink channel modeling using various propagation models at the 3.6 GHz band,” *Radioengineering*, vol. 34, no. 4, pp. 603–623, Dec. 2025. DOI: 10.13164/re.2025.0603
- [11] M. Okano, Y. Hasegawa, K. Kanai, B. Wei, and J. Katton, “Field experiments of 28 GHz band 5G system at indoor train station platform,” in *2020 IEEE 17th Annual Consumer Communications & Networking Conference (CCNC)*, Jan. 2020, pp. 1–6. DOI: 10.1109/CCNC46108.2020.9045247
- [12] 5G-SMART, “Report on 5G radio deployability in the factory,” 5G for Smart Manufacturing, Deliverable 4.2, May 31, 2022.
- [13] M. Cantero, S. Inca, A. Ramos, M. Fuentes, D. Martín-Sacristán, and J. F. Monserrat, “System-level performance evaluation of 5G use cases for industrial scenarios,” *IEEE Access*, vol. 11, pp. 37778–37789, 2023. DOI: 10.1109/ACCESS.2023.3266981
- [14] A. Vijayan *et al.*, “5G wireless channel characterization in indoor factory environments: Simulation and validation,” in *2023 IEEE Wireless Communications and Networking Conference (WCNC)*, Mar. 2023, pp. 1–6. DOI: 10.1109/WCNC55385.2023.10118661
- [15] L. Polak, J. Kufa, R. Sotner, and T. Fryza, “Measurement and analysis of 4G/5G mobile signal coverage in a heavy industry environment,” *Sensors*, vol. 24, no. 8, p. 2538, Jan. 2024. DOI: 10.3390/s24082538
- [16] R. Hernangómez *et al.*, “Toward an AI-enabled connected industry: AGV communication and sensor measurement datasets,” *IEEE Communications Magazine*, vol. 62, no. 4, pp. 90–95, Apr. 2024. DOI: 10.1109/MCOM.001.2300494
- [17] W. Tärneberg *et al.*, “Towards intelligent industry 4.0 5G networks: A first throughput and QoE measurement campaign,” in *2020 International Conference on Software, Telecommunications and Computer Networks (SoftCOM)*, Split, Croatia: IEEE, Sep. 17, 2020, pp. 1–6. DOI: 10.23919/SoftCOM50211.2020.9238299
- [18] S. Santra, L. B. Paet, M. Laine, K. Yoshida, and E. Staudinger, “Experimental validation of deterministic radio propagation model developed for communication-aware path planning,” in *2021 IEEE 17th International Con-*

- ference on Automation Science and Engineering, CASE 2021, IEEE Computer Society, Aug. 23, 2021, pp. 1241–1246. DOI: 10.1109/CASE49439.2021.9551653
- [19] B. Coll-Perales *et al.*, “End-to-end V2X latency modeling and analysis in 5G networks,” *IEEE Transactions on Vehicular Technology*, pp. 1–15, 2022. DOI: 10.1109/TVT.2022.3224614
- [20] R.-G. Lazar, A.-V. Militaru, C.-F. Caruntu, C. Pascal, and C. Patachia-Sultanoiu, “Real-time data measurement methodology to evaluate the 5G network performance indicators,” *IEEE Access*, vol. 11, pp. 43 909–43 924, 2023. DOI: 10.1109/ACCESS.2023.3271366
- [21] M. Costa, D. Ayanda, B. Sátiro, D. Mate, and A. Ortega, “Throughput slopes prediction in 5G networks with gaussian regression process,” in *2023 16th International Conference on Signal Processing and Communication System (ICSPCS)*, Sep. 2023, pp. 1–5. DOI: 10.1109/ICSPCS58109.2023.10261145
- [22] A. Muralidharan and Y. Mostofi, “Communication-aware robotics: Exploiting motion for communication,” *Annual Review of Control, Robotics, and Autonomous Systems*, vol. 4, no. 1, pp. 115–139, 2021. DOI: 10.1146/annurev-control-071420-080708
- [23] S. Caccamo, R. Parasuraman, L. Freda, M. Gianni, and P. Ögren, “RCAMP: A resilient communication-aware motion planner for mobile robots with autonomous repair of wireless connectivity,” in *2017 IEEE/RSJ International Conference on Intelligent Robots and Systems (IROS)*, Sep. 2017, pp. 2010–2017. DOI: 10.1109/IROS.2017.8206020
- [24] U. Ali, H. Cai, Y. Mostofi, and Y. Wardi, “Motion-communication co-optimization with cooperative load transfer in mobile robotics: An optimal control perspective,” *IEEE Transactions on Control of Network Systems*, vol. 6, no. 2, pp. 621–632, Jun. 2019. DOI: 10.1109/TCNS.2018.2863048
- [25] Z. Liu, B. Wu, J. Dai, and H. Lin, “Distributed communication-aware motion planning for networked mobile robots under formal specifications,” *IEEE Transactions on Control of Network Systems*, vol. 7, no. 4, pp. 1801–1811, Dec. 2020. DOI: 10.1109/TCNS.2020.3000742
- [26] X. Mu, Y. Liu, L. Guo, J. Lin, and R. Schober, “Intelligent reflecting surface enhanced indoor robot path planning: A radio map-based approach,” *IEEE Transactions on Wireless Communications*, vol. 20, no. 7, pp. 4732–4747, Jul. 2021. DOI: 10.1109/TWC.2021.3062089
- [27] T. Sarkar, Z. Ji, K. Kim, A. Medouri, and M. Salazar-Palma, “A survey of various propagation models for mobile communication,” *IEEE Antennas and Propagation Magazine*, vol. 45, no. 3, pp. 51–82, Jun. 2003. DOI: 10.1109/MAP.2003.1232163
- [28] C.-X. Wang, J. Bian, J. Sun, W. Zhang, and M. Zhang, “A survey of 5G channel measurements and models,” *IEEE Communications Surveys & Tutorials*, vol. 20, no. 4, pp. 3142–3168, 2018. DOI: 10.1109/COMST.2018.2862141
- [29] H. Qin and X. Zhang, “Efficient Modeling of Radio Wave Propagation in Tunnels for 5G and Beyond Using a Split-Step Parabolic Equation Method,” in *2021 XXXIVth General Assembly and Scientific Symposium of the International Union of Radio Science (URSI GASS)*, Aug. 2021, pp. 1–3. DOI: 10.23919/URSIGASS51995.2021.9560234
- [30] S. Bi, J. Lyu, Z. Ding, and R. Zhang, “Engineering radio maps for wireless resource management,” *IEEE Wireless Communications*, vol. 26, no. 2, pp. 133–141, Apr. 2019. DOI: 10.1109/MWC.2019.1800146
- [31] S. E. Olukanni, I. Risi, S. F. U, and J. O. S, “A gaussian process regression model to predict path loss for an urban environment,” *International Journal of Mathematical Sciences and Computing*, vol. 9, no. 2, p. 10, May 2023.
- [32] T. Kallehauge, “Spatial prediction of wireless channel statistics and its applications to ultra-reliable communication,” Aalborg University, 2024. DOI: 10.54337/aau754337464
- [33] A. AlNasrallah and H. Meng, *R1 EP5G channel measurement*, Zenodo, Jul. 8, 2025. DOI: 10.5281/zenodo.15302998
- [34] C. E. Rasmussen and C. K. I. Williams, *Gaussian Processes for Machine Learning* (Adaptive Computation and Machine Learning). Cambridge, Massachusetts: MIT Press, 2008.
- [35] D. Duvenaud, “Automatic model construction with Gaussian processes,” University of Cambridge, Jun. 2014. DOI: 10.17863/CAM.14087
- [36] Y. Xie, C. Zhu, W. Jiang, J. Bi, and Z. Zhu, “Analyzing machine learning models with Gaussian process for the indoor positioning system,” *Mathematical Problems in Engineering*, vol. 2020, no. 1, p. 4 696 198, 2020. DOI: 10.1155/2020/4696198
- [37] I. Salahshoori, A. Yazdanbakhsh, and A. Baghban, “Machine learning-powered estimation of malachite green photocatalytic degradation with NML-BiFeO₃ composites,” *Scientific Reports*, vol. 14, no. 1, p. 8676, Apr. 15, 2024. DOI: 10.1038/s41598-024-58976-x
- [38] J. Rossmann, M. J. Kamper, and C. M. Hackl, “A generic single-objective machine design framework utilizing gaussian process regression and bayesian optimization,” *IEEE Transactions on Energy Conversion*, vol. 40, no. 1, pp. 677–689, Mar. 2025. DOI: 10.1109/TEC.2024.3452935
- [39] KTH. “History of the KTH Reactor Hall,” Discover KTH, Accessed: Mar. 6, 2026. [Online]. Available: <https://www.kth.se/en/om/upptack/r1/historik-om-kth-reaktorhallen-1.699973>
- [40] S. Mostafavi *et al.*, “ExPECA: An experimental platform for trustworthy edge computing applications,” in *Proceedings of the Eighth ACM/IEEE Symposium on Edge Computing*, Wilmington, DE: ACM, Dec. 6, 2023, pp. 294–299. DOI: 10.1145/3583740.3626819
- [41] Jann Lipka. “Reaktor1 KTH Entrance View 360 Panorama,” 360Cities, Accessed: Dec. 15, 2025. [Online]. Available: <https://www.360cities.net/image/reaktor1-kth-entrance-eqr5300>
- [42] R. Hoppe, G. Wölfle, and U. Jakobus, “Wave propagation and radio network planning software WinProp added to the electromagnetic solver package FEKO,” in *2017 International Applied Computational Electromagnetics Society Symposium - Italy (ACES)*, Mar. 2017, pp. 1–2. DOI: 10.23919/ROPACES.2017.7916282
- [43] I. Felldin. “En dag på Adapt är sig sällan lik en annan,” LinkedIn, Accessed: Oct. 22, 2025. [Online]. Available: https://www.linkedin.com/posts/3disak_en-dag-p%C3%A5-adapt-%C3%A4r-sig-s%C3%A4llan-lik-en-annan-activity-6889186381873119233-MSBJ
- [44] 3GPP, “Physical layer procedures for control,” Sophia Antipolis, France, Technical Specification 38.213, Mar. 30, 2023.
- [45] Husarnet sp. z o.o. “Operate at the edge of latency,” Accessed: Oct. 20, 2025. [Online]. Available: <https://husarnet.com/docs/>
- [46] 3GPP, “User equipment radio access capabilities,” Sophia Antipolis, France, Technical Specification 38.306, Mar. 30, 2023.

- [47] Quectel Wireless Solutions Co., Ltd., “RG50xQ-RM5xxQ Series AT Commands Manual v1.2,” Documentation, Aug. 9, 2021.
- [48] F. Pedregosa *et al.*, “Scikit-learn: Machine learning in python,” *Journal of Machine Learning Research*, vol. 12, no. 85, pp. 2825–2830, 2011.
- [49] F. Cramer, *Scientific colour maps*, version 8.0.1, Zenodo, Oct. 5, 2023. DOI: 10.5281/ZENODO.1243862
- [50] I. Ahmed *et al.*, “A survey on hybrid beamforming techniques in 5G: Architecture and system model perspectives,” *IEEE Communications Surveys & Tutorials*, vol. 20, no. 4, pp. 3060–3097, 2018. DOI: 10.1109/COMST.2018.2843719
- [51] B. Bojovic and S. Lagen. “MIMO in network simulators: Design, implementation and evaluation of single-user MIMO in ns-3 5G-LENA.” arXiv: 2404.17472 [cs], Accessed: Jan. 27, 2026. [Online]. Available: <http://arxiv.org/abs/2404.17472> pre-published.